Nano Research

Open Access

Research Article

High-selective Fischer–Tropsch synthesis to jet fuel over confined iron catalysts inside carbon nanocages

Fujie Gao[1], Xinyi Wang[1], Ou Zhuo[2], Changkai Zhou[1], Lijun Yang[1], Qiang Wu[1], Yining Fan[1], Xizhang Wang[1]✉, Hongwen Huang[1]✉, and Zheng Hu[1]✉

[1] *Key Laboratory of Mesoscopic Chemistry of MOE and Jiangsu Provincial Laboratory for Nanotechnology, School of Chemistry and Chemical Engineering, Nanjing University, Nanjing 210023, China*
[2] *College of Chemistry and Chemical Engineering, Jishou University, Jishou 416000, China*

Cite this article: *Nano Research*, **2025**, *18*, 94907331. https://doi.org/10.26599/NR.2025.94907331

ABSTRACT: Selective production of specific products, such as jet fuel, in Fischer–Tropsch synthesis (FTS) is a huge challenge due to the Anderson–Schulz–Flory (ASF) distribution law. Herein, by filling K-promoted Fe-based active species, which usually produces medium-to-short chain hydrocarbons in high-temperature FTS, into the hierarchical carbon nanocages (hCNC), jet fuel with high selectivity of 60% is directly obtained in FTS at 300 °C, exceeding the ASF maximum limitation of ca. 41%. Through the theoretical simulations, we attribute this performance to the CO enrichment inside the nanocavities due to the sieving effect of the micropores across the hCNC shells (~ 6 Å) and the increased collision frequency in confined space. These two factors thereby promote the CO conversion and carbon-chain growth longer over the catalytically active Fe_5C_2 phase, resulting in the remarkable selectivity to jet fuel. The effects of the length and size of micropores on the CO/H_2 diffusion and FTS performance are examined, which corroborate the crucial role of micropores in the high-selective FTS to jet fuel. This work not only provides a remarkable catalyst to the selective jet fuel synthesis, but also offers an alternative way to design advanced catalysts for FTS.

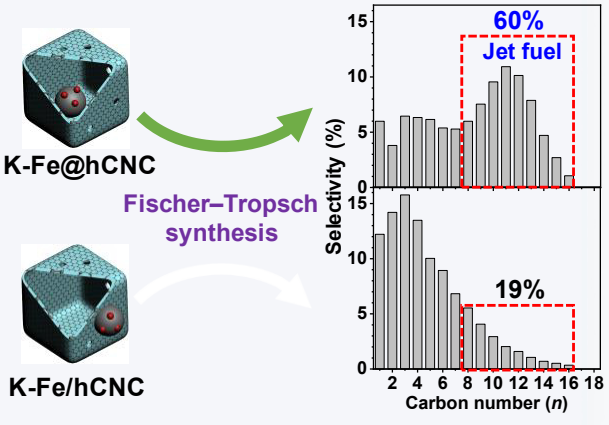

KEYWORDS: Fischer–Tropsch synthesis, confined iron catalysts, jet fuel, Anderson–Schulz–Flory distribution, hierarchical carbon nanocages

1 Introduction

Jet fuel (a mixture of C_8–C_{16} hydrocarbons) is an indispensable and hugely-consumed fuel in aviation industry [1], which is now mainly produced from the distillation or cracking of crude oil [2]. In view of the high pollution of this process and the exhaustion of oil resources, sustainable production of jet fuel is highly desirable. Fischer–Tropsch synthesis (FTS) that can convert the syngas (from natural gas, coal, biomass, etc.) into high value-added liquid fuels and chemicals in large quantities should be a suitable choice to produce jet fuel with much reduced environmentally unfriendly impurities (e.g. sulfur-containing and aromatic compounds) and NO_x/particulates emissions [3]. However, the FTS to jet fuel remains elusive with rare reports, and only Co-based catalysts favorable for carbon chain propagation have been explored to date [4–6]. In general, the hydrocarbon products of FTS obey the Anderson–Schulz–Flory (ASF) distribution, and the theoretical maximal selectivity for jet fuel is ca. 41% [6, 7]. By employing 1-olefins as additional inducer for FTS to initiate new carbon chain propagation, Tsubaki et al. achieved an ultrahigh selectivity of jet fuel up to 64%–83.3% [8, 9]. However, adding large amounts of the expensive 1-olefin will much increase the production cost of jet fuel, unfavorable for practical applications. Subsequently, by filling Co nanoparticles into the nanochannels of La^{3+}-exchanged mesoporous Y-type zeolite (Co/Y_{meso}-La), the same research group obtained a high selectivity of 72% for jet fuel without needing the additional 1-olefins inducer. Here, the suitable acidity and mesopore size of

Received: January 16, 2025; **Revised:** February 18, 2025
Accepted: February 25, 2025

✉Address correspondence to Xizhang Wang, wangxzh@nju.edu.cn; Hongwen Huang, huanghw@nju.edu.cn; Zheng Hu, zhenghu@nju.edu.cn

Y_{meso}-La leads to the modest hydrocracking of the Fischer–Tropsch wax formed on Co metal, thereby a high selectivity for jet fuel [5]. Actually, confining active species inside a limited space has become an effective strategy to explore advanced catalysts for different reactions [10–17]. Among them, the confinement effect of carbon nanotube (CNT) and mesoporous silica has already regulated the catalytic performance via changing the electronic environment of the catalyst or using spatial confinement effect on diffusion behavior of reactant/product in FTS [10–12]. However, they have not been used for highly selective jet fuel production for the restricted channel of CNT and the inconvenience of adjusting pore structures of SiO_2.

In recent years, we have developed the hierarchical carbon nanocages (hCNC) consisting of the building units of carbon nanocages, which presents the flower-like architecture with co-existing micro-, meso-, and macropores. The hollow nanocavities and abundant micropores across the shells of carbon nanocages enable the convenient encapsulation of different alien species, while the multiscale porous structure ensures the rapid mass transportation [18]. Taking these advantages, in this study we encapsulated the iron-based active species, which usually produces medium-to-short chain hydrocarbons in high-temperature FTS [19, 20], into the hCNC to construct the confined Fe@hCNC catalysts by a vacuum-filling method. The optimized K-promoted catalyst, K-Fe@hCNC, delivers a high selectivity of 60% for jet fuel in FTS at 300 °C, which is much superior to the ASF maximum (ca. 41%) and also significantly higher than 19% for the supported counterpart of K-Fe/hCNC catalyst under the similar CO conversion of ~ 58%. The excellent catalytic performance is attributed to the CO enrichment inside the nanocavities due to the sieving effect of the micropores across the hCNC shells and the increased collision frequency in confined space. This study provides a promising strategy to break the ASF distribution and increase the specific high value-added products via constructing the confined catalysts using the unique support of hierarchical carbon-based nanocages.

2 Experimental

2.1 Catalysts preparation

The hCNC supports were prepared by the *in-situ* MgO template method at 800 °C with benzene precursor, similar to our previous reports. Before removing MgO template, the inner cavities of hCNC are completely occupied by MgO, denoted as MgO@hCNC (Fig. S1 in the Electronic Supplementary Material (ESM)). The wall-thickness of hCNC was tuned by changing the benzene dosage, and the hCNC samples with a thinner or thicker shell thickness were obtained, denoted as hCNC-1 and hCNC-2. hCNC treated with dilute nitric acid was denoted as hCNC-L (Fig. S2 in the ESM).

The confined catalyst was prepared by vacuum-filling process and the supported catalyst was prepared by impregnation method, as illustrated in Fig. 1(a). Typically, a sealed vessel containing 200 mg hCNC was vacuumized to ca. 5 Pa, and then 20 mL solution of $Fe(NO_3)_3{\cdot}9H_2O$ (0.8 mol·L^{-1}) containing 0.1 mL of nitric acid (HNO_3, ~ 68 wt.%) were quickly added into the vessel, followed by the magnetic stirring for 2 h. The suspension was filtrated, freeze-dried, and then heat-treated at 360 °C in Ar for 2 h, denoted as pre-Fe@hCNC. The Fe species outside the nanocages was removed by leaching with dilute nitric acid, denoted as Fe@hCNC. Then, K is added into Fe@hCNC with the same the filling process by replacing the $Fe(NO_3)_3$ solution with KNO_3

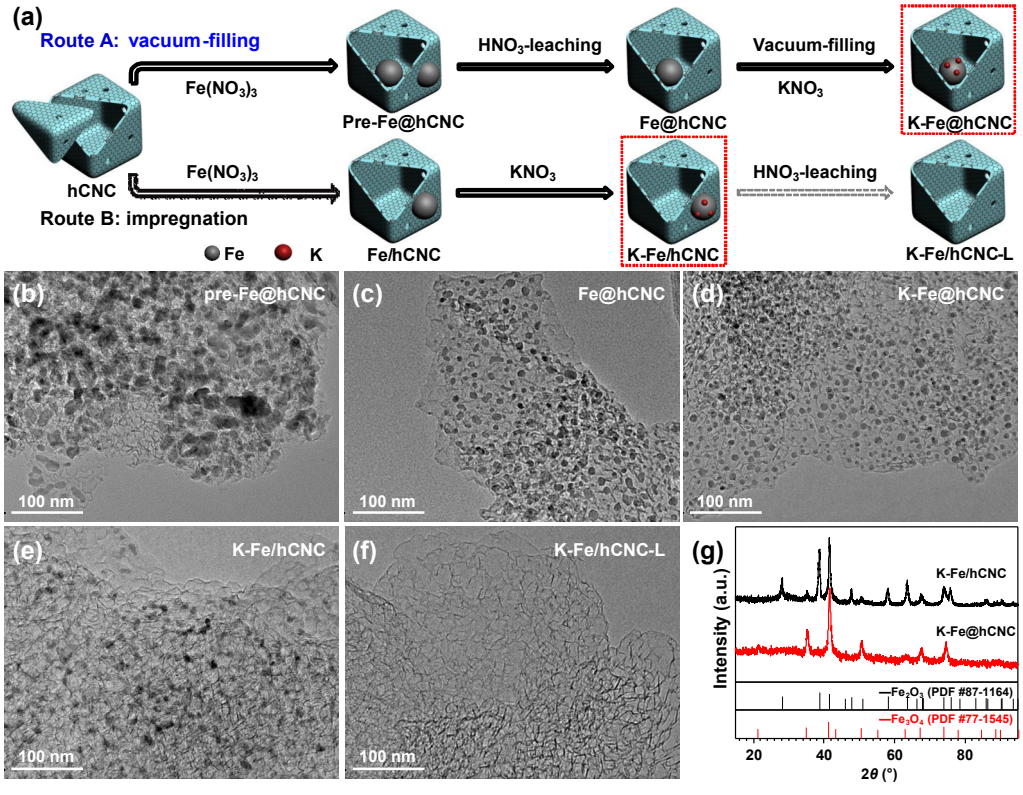

Figure 1 Preparation and characterization of the confined and supported catalysts. (a) Schematic diagram of preparation process. TEM images of (b) pre-Fe@hCNC, (c) Fe@hCNC, (d) K-Fe@hCNC, (e) K-Fe/hCNC, and (f) K-Fe/hCNC-L. (g) XRD patterns.

solution (3 mmol·L^{-1}). The resultant confined catalyst is denoted as K-Fe@hCNC (Route A). The supported K-Fe/hCNC control catalyst was synthesized Route B. Specifically, 200 mg hCNC was first ultrasonically dispersed in 15 mL deionized water for 1 h. Then 3 mL ferric nitrate solution was dropwise added to the suspension at 60 °C and magnetically stirred for 2 h. After the solvent evaporated, the powder was heat-treated at 360 °C in Ar for 2 h to obtain the Fe/hCNC. Then KNO_3 solution was added by the similar impregnation steps to introduce K, labelled as K-Fe/hCNC. For comparison, K-Fe/hCNC was also leached with dilute nitric acid, labelled as K-Fe/hCNC-L. By replacing hCNC with hCNC-1, hCNC-2 and hCNC-a, K-Fe@hCNC-1, K-Fe@hCNC-2 and K-Fe@hCNC-a were obtained.

2.2 Materials characterizations

The catalysts were characterized by high-resolution transmission electron microscopy (HRTEM, JEM-2100, operating at 200 kV), X-ray diffraction (XRD, Bruker D8 Advance A25, Co Kα1 radiation of 1.78897 Å with Fe filter of 0.02 mm thickness), X-ray photoelectron spectroscopy (XPS, ULVAC-PHI INC, PHI 5000 Versa Probe, Al Kα), and H_2 temperature-programmed reduction (H_2-TPR, 20 mL·min^{-1} 5 vol.%. H_2/Ar flow at a temperature ramping rate of 10 °C·min^{-1} up to 800 °C), respectively. N_2 adsorption/desorption isotherm was measured on Thermo Fisher Scientific Surfer Gas Adsorption Porosimeter at 77 K after degassed at 300 °C for 6 h. The specific surface area and pore distribution was calculated using the Brunauer–Emmett–Teller (BET), Horvath–Kawazoe (H–K, for < 2 nm micropores) and Barrett–Joyner–Halenda (BJH, for > 2 nm meso-macro-pores) methods based on the data of adsorption branch. The iron loadings were measured by the thermogravimetric analysis (TGA, Netzsch STA-449F3) in 10 vol.% O_2-containing argon flow of 20 mL·min^{-1} at a temperature ramping rate of 10 °C·min^{-1}.

For CO-TPD, 100 mg sample was reduced reduce at 420 °C by 10 vol.% H_2/Ar flow for 1.5 h. Then CO was adsorbed at room temperature for 1 h and subsequently purged with He until a stable baseline was achieved. The CO-TPD curve was recorded by quadruple mass spectrometer (AMETEK DYCOR DME300MS, m/z = 28) from room temperature to 800 °C at a heating rate of 10 °C·min^{-1}.

In-situ diffuse reflection infrared spectroscopy (DRIFTS) for CO adsorption intensity with catalysts were conducted in BRUKER TENSOR II IR instrument with a liquid nitrogen cooled MCT detector. Spectra were measured from 4000 to 1000 cm^{-1} wavenumbers with 32 scans at a resolution of 4 cm^{-1}. DRIFTS for analysis of the reaction process were conducted in Thermo Scientific Nicolet iS50 instrument with a liquid nitrogen cooled MCT/A detector. Spectra were measured from 4000 to 650 cm^{-1} wavenumbers with 64 scans at a resolution of 8 cm^{-1}. Before all testing, the samples of equal mass diluted with potassium bromide in the same ratio were reduced with 10 vol.% H_2/Ar at 420 °C and purged with Ar at 300 °C for 1 h. During the cooling process, baselines at different temperatures are recorded. Then CO was adsorbed at atmosphere pressure, and purged with Ar at different temperatures. The reaction process is analyzed by exposed K-Fe@hCNC or K-Fe/hCNC in CO/H_2 (1/1) at 300 °C and 0.2 MPa.

2.3 Catalytic evaluation

FTS reactions were performed at 2.0 MPa and 300 °C in a fixed-bed micro-reactor. 50 mg catalyst was diluted with 3.0 g of quartz sand (40–60 mesh) to achieve isothermal plug-flow conditions and then charged into a passivated stainless-steel tube reactor. The catalyst was in situ reduced at 420 °C under 10 vol.% H_2/Ar flow (20 sccm) for 1.5 h, then cooled down to 300 °C. The gas mixture of H_2/CO/Ar (47.5/47.5/5.0) was fed into the reactor at a certain flow rate, with Ar as an internal standard. C_1–C_4 and C_5–C_{30} hydrocarbons were analyzed by gas chromatography (Qiyang GC9860) equipped with PLOT-Al_2O_3 and HP-PONA capillary columns connected to flame ionization detector (FID), respectively. A hot trap is equipped to collect the wax, and the pipeline is maintained at 180 °C to allow comprehensive on-line product analysis. High boiling point hydrocarbons are analysed using an Agilent HP-5 chromatography column with a temperature program that can reach up to 300 °C. Ar, CO, CO_2, CH_4 were detected by GC9860 equipped with TDX-01 column connected to thermal conductivity detector (TCD). The hydrocarbons selectivity was calculated on the carbon basis.

Carbon balance was calculated as Eq. (1)

$$\text{Carbon balance} = \frac{\sum \text{HC}_{\text{online}} + \sum \text{HC}_{\text{offline}} + \text{CO}_2}{\text{CO}_{\text{in}} - \text{CO}_{\text{out}}} \times 100\% \quad (1)$$

The amount of CO consumption and CO_2 generation in FTS were measured by TCD, the gas phase products (gaseous hydrocarbons, HC_{online}) were detected by a gas chromatograph equipped with a flame ionization detector, and the liquid phase products ($HC_{offline}$) collected in the cold trap were detected by another gas chromatograph equipped with a flame ionization detector. After the reaction reached the stable stage, the whole carbon balances were better than 90%.

Turnover frequency (TOF) was calculated as Eq. (2)

$$\text{TOF} = \frac{\text{the number of CO converted}}{\text{reaction time} \times \text{the number of active sites}} \quad (2)$$

The number of CO molecules of the converted reactant can be calculated by the flow rate of the feedstock gas and the conversion rate of the catalyst, the reaction time is 1 s, and the number of active sites is calculated by CO pulse chemisorption measurements [21].

3 Results and discussion

3.1 Structure and composition characterizations

The hCNC possess nanocavities of 10–30 nm in size, along with abundant micro-meso-macropores, the removal of the template causes little structural damage in its morphology (Figs. S1 and S2 in the ESM). Figure 1 shows the preparation and characterizations on the prepared catalysts. During the preparation of K-Fe@hCNC (Route A in Fig. 1(a)), the iron nanoparticles exist both inside and outside the nanocages for the pre-Fe@hCNC intermediate (Fig. 1(b)). After leaching pre-Fe@hCNC with dilute nitric acid, the outside iron nanoparticles were removed and the substantial inside iron nanoparticles remain there for Fe@hCNC (Fig. 1(c)), and the K-modified confined catalyst of K-Fe@hCNC was obtained by adding K (Fig. 1(d)). On the contrary, for the K-Fe/hCNC (Route B in Fig. 1(a)), all the iron nanoparticles are dispersed on the outer surface of hCNC, as verified by the complete removal of nanoparticles by the nitric acid leaching (Figs. 1(e) and 1(f)). Hence, K-Fe@hCNC and K-Fe/hCNC provide a pair of counterparts with the iron nanoparticles inside and outside the cavities of hCNC, respectively. The Fe component mainly exists in the form of Fe_3O_4

for K-Fe@hCNC and in Fe_2O_3 for K-Fe/hCNC with a close Fe content/particle size of 39.2 wt.%/9.9 ± 2.5 nm and 38.1 wt.%/9.0 ± 2.5 nm (31.3 wt.% and 33.0 wt.% by ICP, Table S1 in the ESM), respectively, which will transform into Fe_xC_y active phase during FTS (Fig. 1(g), Figs. S3 and S4 in the ESM) [22]. Both catalysts exhibit a decrease of pore volume as expected due to the partial occupation/occlusion of the meso-/micro-pores by the iron nanoparticles (Fig. S5 in the ESM). It is noteworthy that the micromorphology and pore structures of hCNC are hardly changed after dilute nitric acid treatment (Figs. S2 and S5 in the ESM) The XPS signal intensity of Fe element for K-Fe@hCNC is much weaker than that for K-Fe/hCNC, due to the exponential attenuation of the signal intensity when penetrating the carbon shells (Fig. S6 in the ESM) [23].

3.2 Catalytic performances

The catalytic performances of K-Fe/hCNC and K-Fe@hCNC are shown in Fig. 2 and Table 1. To ensure the catalytic reaction within the kinetic range, the influence of gas hourly space velocity (GHSV) on the catalytic performance was examined for K-Fe@hCNC. As GHSV decreases from 24,000 through 18,000, 12,000 to 6000 mL·h^{-1}·g^{-1}, the CO conversion gradually increases from 30% through 41%, 58% to 88%, respectively, with similar product distributions (Fig. S7 in the ESM). Hence, when GHSV is higher than 12,000 mL·h^{-1}·g^{-1}, the catalytic reaction of K-Fe@hCNC locates in the kinetic range with the TOF of ~ 1.5 s^{-1} [24].

K-Fe@hCNC exhibits much higher catalytic activity and selectivity for producing C_8–C_{16} (jet fuel) than K-Fe/hCNC. Specifically, at the CO conversion of ~ 58%, the TOF of K-Fe@hCNC is 7.5 times greater than that of K-Fe/hCNC, with the product distributions centered at C_{11} for the former and at C_3 for the latter (Figs. 2(a) and 2(b) and Table 1). The selectivity for C_8–C_{16} products achieves 60% for K-Fe@hCNC, exceeding the ASF limit value of 41% [6, 7], also much higher than 19% for K-

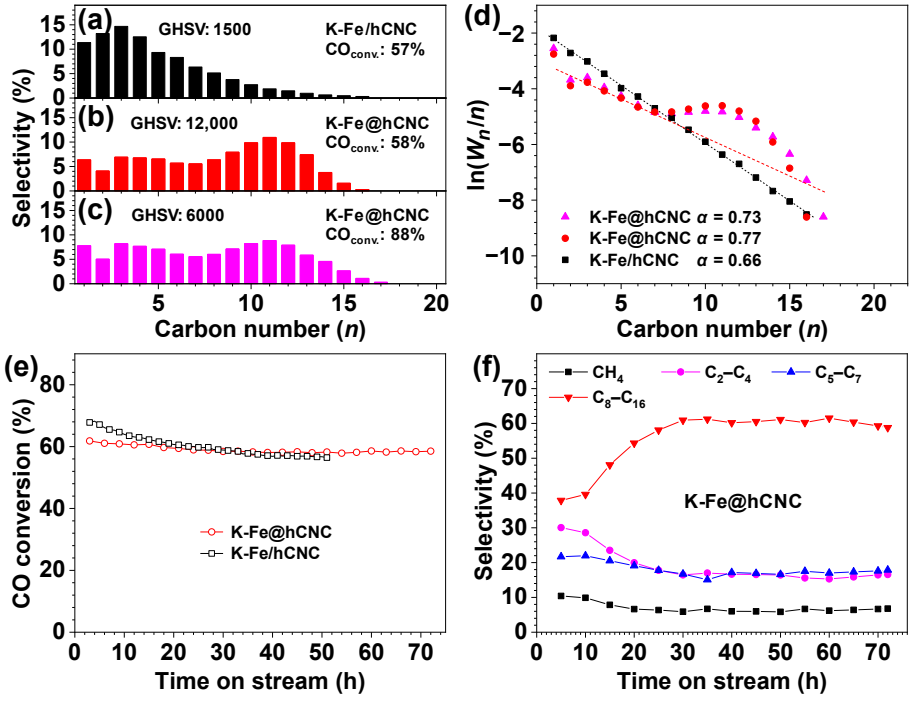

Figure 2 Catalytic performances for K-Fe@hCNC and K-Fe/hCNC. (a)–(c) Histograms of hydrocarbon product selectivity vs. carbon number (n). (d) Plots of ln(W_n/n) vs. n. (e) CO conversion vs. time on stream (TOS). Data of K-Fe/hCNC is plotted for comparison. (f) Selectivity of designated products vs. TOS. Reaction conditions: 300 °C, 2 MPa, H_2/CO = 1, GHSV: mL·h^{-1}·g^{-1}. The data in (a)–(d) are taken at TOS = 45 h.

Table 1 Catalytic performances of the supported and confined catalysts in FTS[a]

Samples	GHSV (mL·h^{-1}·g^{-1})	CO conversion (%)	TOF (s^{-1})[b]	Hydrocarbon distribution (at.% of C)				
				CH_4	C_2–C_4	C_5–C_7	C_8–C_{16}	C_{16+}
K-Fe/hCNC	1500	57	0.2	12	43	26	19	—
K-Fe@hCNC	6000	88	1.1	8	21	19	52	< 1
	12,000	58	1.5	6	17	17	60	—
	18,000	41	1.6	6	16	16	62	—
	24,000	30	1.5	6	16	17	60	—
K-Fe@hCNC-1	3000	61	0.4	6	30	21	44	—
K-Fe@hCNC-2	5000	63	0.7	3	18	13	59	6
K-Fe@hCNC-a	5000	57	0.6	19	29	17	35	—

[a] Reaction conditions: 300 °C, 2 MPa, H_2/CO = 1, TOS = 45 h. [b] TOF: moles of CO converted to hydrocarbons per mole of surface sites per second.

Fe/hCNC. In addition, the selectivity of CH_4 and C_2–C_4 are only 6% and 17% for K-Fe@hCNC, much lower than the corresponding 12% and 43% for K-Fe/hCNC (Table 1). Such yield of jet fuel for K-Fe@hCNC is at the top level compared with other catalysts (Fig. S8 and Table S2 in the ESM).

According to the ASF distribution law, there is a linear relationship between $\ln(W_n/n)$ and n: $\ln(W_n/n) = n\ln\alpha + \ln((1-\alpha)^2/\alpha)$, where W_n is the weight fraction of the product with a carbon number of n. Hence, the slope of this linear equation can be used to evaluate the chain growth possibility (α). For K-Fe/hCNC, a linear relationship of $\ln(W_n/n)$ versus n is observed across the entire range of products, indicating an ASF distribution, with an α value of 0.66 (Fig. 2(d)). In contrast, for K-Fe@hCNC, the relationship of $\ln(W_n/n)$ versus n is linear only in the range of C_3–C_7, with an α value of 0.77.

The selectivity for C_8–C_{15} is significantly higher than the theoretical value of the ASF distribution with a large deviation (Fig. 2(d)). The active phase of K-Fe@hCNC and K-Fe/hCNC is Fe_5C_2, which is an active phase for FTS and plays a crucial role in the C–C chain growth reactions (Fig. S9 in the ESM) [25, 26]. As a comparison, without K promoter, the selectivity of jet fuel for Fe@hCNC and Fe/hCNC are only 24% and 8%, respectively, indicating the promotion effect of K for the formation of the Fe_5C_2 active phase and carbon chain propagation (Fig. S10 and Table S3 in the ESM) [3, 27].

The catalytic stability of K-Fe@hCNC are examined, as shown in Figs. 2(e) and 2(f). The CO conversion slightly decreases from the initial ~ 62% to ~ 58% within 72 h, demonstrating the enhanced catalytic stability to the control catalyst of K-Fe/hCNC (Fig. 2(e)). This result could be attributed to the slower iron carbonyl-mediated growth of Fe_5C_2 nanoparticles for K-Fe@hCNC than K-Fe/hCNC [21], due to the confined Fe_5C_2 active-phase and iron carbonyl for the former (Figs. S11 and S12 in the ESM). In the initial 30 h, the selectivities of short-chain products (CH_4 and C_2–C_4) obviously decrease, while those of long-chain products (C_8–C_{16}) obviously increase, and that of middle-chain product (C_5–C_7) slightly fluctuates, then selectivities of these products achieve a relatively stable state (Fig. 2(f)). This observation can be ascribed to the increasing size of Fe_5C_2 nanoparticles (Fig. S11 in the ESM), as the small-sized Fe_5C_2 nanoparticles tend to produce the short-chain products while the large-sized Fe_5C_2 nanoparticles tend to favor heavy hydrocarbons (C_{5+}) [24, 28]. In addition, the K-Fe@hCNC-spent showed almost no carbon deposits on the surface, less decrease in pore volume, and less K loss than K-Fe/hCNC-spent, which is consistent with its better stability results (Figs. S11–S13 and Table S1 in the ESM) [29].

3.3 Theoretic simulations of the diffusion and collision behaviors

The proceeding results indicate that the confined K-Fe@hCNC catalyst has far higher catalytic activity and jet fuel selectivity than the supported K-Fe/hCNC, with an evident deviation from the ASF distribution law for the product distribution. This situation can be attributed to the unique diffusion process of reactant/product in/out of the nanocavities of the confined K-Fe@hCNC catalyst given the same active phase used in two cases. Hence, we conducted theoretical simulation study on the diffusion behavior of CO/H_2 molecules through micropores across the hCNC shells and the collision frequency between CO and Fe_5C_2 nanoparticles in confined space.

To simulate the diffusion behavior of CO/H_2 molecules in hCNC, the fullerene-like carbon nanosphere was used to imitate the carbon nanocage unit, with a diameter of 2.5 nm and ~ 6 Å micropore. Two carbon nanospheres were connected through micropore as diffusion model of CO/H_2 molecules in hCNC, as shown in Fig. 3. The syngas with a CO/H_2 ratio of 1:1 was placed at one side of the diffusion model, and the syngas would diffuse through the model to the other end after relaxation equilibrium. With the simulation time going, the number of CO/H_2 molecules inside the nanospheres gradually increased and then reached a relatively stable state with an increased CO/H_2 ratio of ca. 2.3:1 (Fig. 3(b) and Fig. S14 in the ESM). This result indicates that CO could enrich inside the nanocages relative to H_2, which is likely related to the sieving effect of micropores (~ 6 Å) through the nanocage shell for CO and H_2 molecules. The H_2 molecules with light weight and small kinetic radius (2.9 Å) can easily go through the nanocages with small hinderance. While for the CO molecules, the relatively large weight and kinetic radius (3.8 Å) make them being hold inside the nanocages for longer time, resulting in higher CO/H_2 ratio inside. Of note, this situation caused by diffusion in nanosphere is different from the enrichment of CO in CNTs caused by electronic effect [30, 31]. In addition, the syngas molecules inside the nanocages frequently collide with the nanocage walls, which also has significant effect on the reactivity.

We constructed a simple hard sphere model to count the collision frequency between the reactant molecules and the Fe_5C_2 particle in the confined or open space with the same gas density (Figs. 3(c) and 3(d) and Table S4 in the ESM). The collision frequency is 1.7 times higher in the confined space than in the open space, which results from the rebound of gas molecules after colliding to the inner wall of nanocage for the former [17, 32]. As a result, the higher concentration of CO and the higher collision frequency between CO and Fe_5C_2 nanoparticles inside the nanocages lead to much higher catalytic activity of K-Fe@hCNC than that of K-Fe/hCNC.

Meanwhile, the chain termination and the probability of olefin to paraffin through hydrogenation are weakened due to relatively poor H_2 atmosphere in the confined space, resulting in the high selectivity of jet fuel and olefin/paraffin (O/P) ratio of C_2–C_5 in FTS for K-Fe@hCNC (Fig. S15 in the ESM). *In-situ* DRIFTS shows that linearly bonded CO (2058 cm^{-1}) gradually disappeared with increasing temperature, indicating that CO was weakly adsorbed on both K-Fe@hCNC and K-Fe/hCNC (Fig. S16 in the ESM) [33]. The signal disappearance temperature on K-Fe@hCNC is higher than that of K-Fe/hCNC, indicating that CO adsorption on K-Fe@hCNC is stronger than that of K-Fe/hCNC. This result is consistent with that of CO-TPD profile for K-Fe@hCNC and K-Fe/hCNC (Fig. S17 in the ESM). Moreover, the time-resolved *in situ* DRIFTS in the condition of CO/H_2 (1/1) atmosphere at 300 °C clearly show that the CH_2 species (2896 and 2968 cm^{-1}) increase faster for K-Fe@hCNC than for K-Fe/hCNC in 0–5 min, revealing the stronger chain growth ability than K-Fe/hCNC (Fig. S18 in the ESM) [34, 35].

3.4 Experimental regulation of micropore parameters

The preceding theoretical simulation results suggest that the high selectivity of jet fuel for the confined K-Fe@hCNC results from the CO enrichment due to the sieving effect of micropores on CO/H_2 gaseous diffusion. For the confined K-Fe@hCNC, the gaseous diffusion to the Fe_5C_2 surface includes sequential steps of the

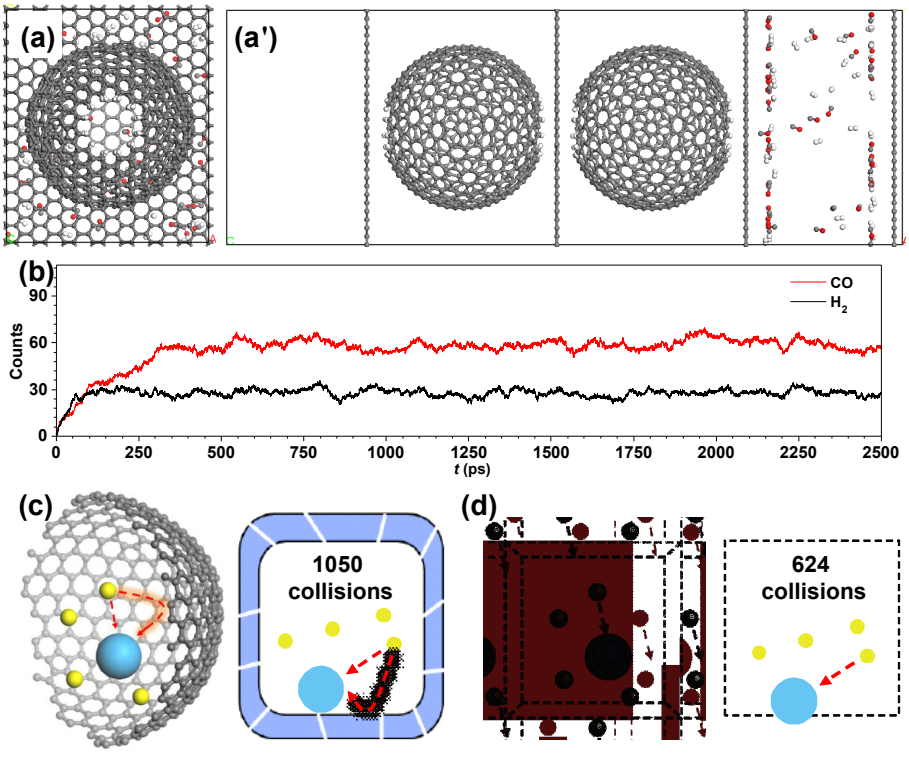

Figure 3 Molecular dynamics simulation. (a) Diffusion model of CO/H_2 molecules in hCNC. (a') The side view of the model. (b) The number of CO and H_2 molecules inside the diffusion model over time. Collision model between reactant molecules and Fe_5C_2 nanoparticle in (c) confined space and (d) open space.

external diffusion outside the nanocages and the internal diffusion into the nanocavities through the micropores [20]. The external diffusion rate depends on GHSV and will not affect the catalytic activity when the catalytic reaction of K-Fe@hCNC locates in the kinetic range. The internal diffusion rate depends on the parameters of the micropores. Thus the microporous parameters such as length, size or number were tuned to further examine the influence of micropores on the CO/H_2 diffusion and the FTS performance thereof.

Three supports of hCNC-1, hCNC and hCNC-2 were prepared, which have the similar pore size distributions but the different micropore length with 2–5, 4–7 and 7–12 carbon layers, respectively (Fig. S2 in the ESM). The corresponding confined catalysts of K-Fe@hCNC-1, K-Fe@hCNC and K-Fe@hCNC-2 with similar morphologies were constructed and applied to FTS, as shown in Fig. 4 and Table 1. Under a similar CO conversion (~ 60%), with increasing the micropore length, the catalytic activity first increased and then decreased, as reflected by the TOF change from 0.4 via 1.5 to 0.7 s^{-1}. Compared with the case of K-Fe@hCNC, the product distribution of K-Fe@hCNC-1 shifts towards lower carbon numbers, and the selectivity of C_8–C_{16} obviously decreases from 60% to 44%, with less deviation from the ASF distribution. As contrast, the product distribution of K-Fe@hCNC-2 shifts towards higher carbon numbers, and the selectivity of C_8–C_{16} almost remains unchanged (59%), with the similar deviation from the ASF distribution (Figs. 4(d) and 4(e)). These results indicate the significant influence of the micropore length on the catalytic activity and product distribution. Specifically, the shorter micropore length of K-Fe@hCNC-1 than K-Fe@hCNC has weaker sieving effect and CO enrichment for K-Fe@hCNC-1, which may decrease the catalytic activity and shift the product distribution to the lower carbon numbers. On the contrary, the longer micropore length of K-Fe@hCNC-2 than K-Fe@hCNC has stronger sieving effect and CO enrichment as well as the larger mass transfer resistance for K-Fe@hCNC-2. As a result, the product distribution of K-Fe@hCNC-2 shifts to the higher carbon numbers with a decreased catalytic activity in comparison with the cases of K-Fe@hCNC.

We also enlarged the micropores of the nanocage using CO_2 etching to examine the effect of micropore size, as shown in Fig. 4 and Table 1. The Boudouard reaction ($C + CO_2 \rightarrow 2CO$) was used to enlarge the micropores to obtain the etched sample of K-Fe@hCNC-a (Figs. S19 and S20 in the ESM) [36, 37]. Compared with K-Fe@hCNC, K-Fe@hCNC-a exhibits the evidently reduced catalytic activity in the similar CO conversion (~ 58%), as reflected by the TOF decrease from 1.5 to 0.6 s^{-1}. Meanwhile, the product distribution shifts towards lower carbon numbers and the selectivity of C_8–C_{16} decreases from 60% to 35% with a delayed deviation from the ASF distribution for C_{10}–C_{15} products, which is attributed to the weakened sieving effect and improved mass transfer of reactants and products through the enlarged micropores (Figs. 4(d) and 4(e)). The trend of jet fuel selectivity variation with micropore parameters is shown in Fig. 4(f). All these results consistently indicate that the high selectivity of jet fuel for the confined K-Fe@hCNC can be attributed to the CO enrichment arising from the sieving effect of micropores on CO/H_2 gaseous diffusion.

4 Conclusions

This study demonstrates the successful preparation of K-promoted Fe nanoparticles confined within the nanocavities of hCNC, or dispersed on the outer surface of hCNC as the counterpart. The optimized confined catalyst, K-Fe@hCNC, delivers 7.5 times higher catalytic activity than that of supported K-Fe/hCNC at the CO conversion of ~ 58%. Meanwhile, the selectivity of jet fuel for K-Fe@hCNC reaches as high as 60%, significantly higher than that of 19% of the supported K-Fe/hCNC catalyst, with an evident

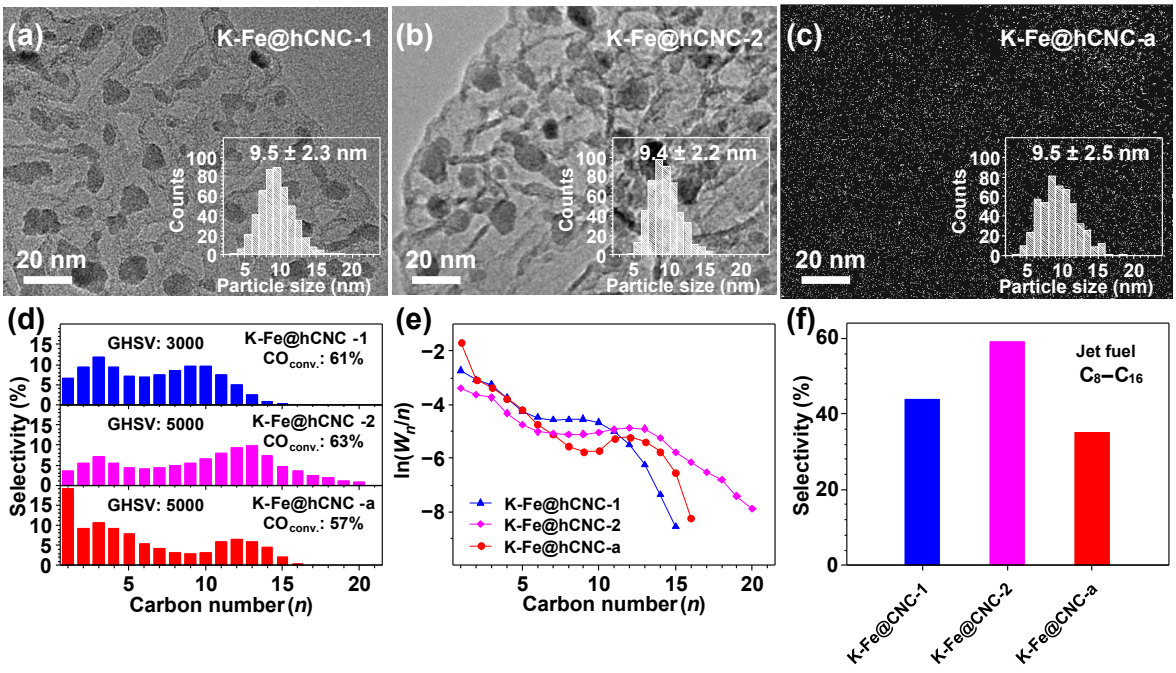

Figure 4 Examination on the sieving effect of micropore length and size of hCNC for the confined FTS catalysts. TEM images and corresponding particle size distributions of (a) K-Fe@hCNC-1, (b) K-Fe@hCNC-2, and (c) K-Fe@hCNC-a. (d) Histograms of product selectivity vs. carbon number (n), (e) plots of $\ln(W_n/n)$ vs. n, and (f) selectivity of jet fuel for K-Fe@hCNC-1, K-Fe@hCNC-2, and K-Fe@hCNC-a. Reaction conditions: 300 °C, 2 MPa, $H_2/CO = 1$, TOS = 45 h. GHSV: mL·h^{-1}·g^{-1}.

deviation from the maximum of ca. 41% for jet fuel in the classical ASF distribution. This situation is associated with the unique diffusion process of reactant/product in/out of the nanocavities of the confined K-Fe@hCNC catalyst. Through the theoretical simulation, we attributed the excellent performance of K-Fe@hCNC to the CO enrichment inside the nanocavities due to the sieving effect of the micropores across the hCNC shells and the increased collision frequency in confined space. The micropore parameters such as their length and size play a critical role in the sieving effect of micropores of the hCNC on CO/H_2 gaseous diffusion, and finally influence the selectivity of jet fuel in FTS. K-Fe@hCNC also demonstrate the superior catalytic stability than K-Fe/hCNC due to the confined Fe_5C_2 active-phase. Confining the active species inside the unique hierarchical carbon-based nanocages could be a general strategy to tune the ASF distribution towards the specific high value-added products.

Electronic Supplementary Material: Supplementary material (additional characterizations and supporting results) is available in the online version of this article at https://doi.org/10.26599/NR.2025.94907331.

Data availability

All data needed to support the conclusions in the paper are presented in the manuscript and the Electronic Supplementary Material. Additional data related to this paper may be requested from the corresponding author upon request.

Acknowledgements

This work was jointly supported by the National Key Research and Development Program of China (No. 2021YFA1500900), the National Natural Science Foundation of China (Nos. 21972061 and 52071174), the Natural Science Foundation of Jiangsu Province, Major Project (No. BK20212005), and the Foundation of Science and Technology of Suzhou (No. SYC2022102).

Declaration of competing interest

All the contributing authors report no conflict of interests in this work.

Author contribution statement

F. J. G.: Conceptualization, data curation, investigation, writing – original draft. X. Y. W.: Software, data curation. O. Z.: Formal analysis. C. K. Z.: Investigation. L. J. Y.: Software,. writing – review & editing. Q. W.: Writing – review & editing. Y. N. F.: Methodology, writing – review & editing. X. Z. W.: Experimental design, writing – review & editing. H. W. H.: Conceptualization, writing – review & editing. Z. H.: Project administration, funding acquisition, writing – review & editing. All the authors have approved the final manuscript.

Use of AI statement

None.

References

[1] Schäppi, R.; Rutz, D.; Dähler, F.; Muroyama, A.; Haueter, P.; Lilliestam, J.; Patt, A.; Furler, P.; Steinfeld, A. Drop-in fuels from sunlight and air. *Nature* **2022**, *601*, 63–68.

[2] Robinson, P. R.; Dolbear, G. E. Hydrotreating and hydrocracking: fundamentals. In *Practical Advances in Petroleum Processing*. Hsu, C. S.; Robinson, P. R. Eds.; Springer: New York, 2006; pp 177–218.

[3] Zhang, Q. H.; Kang, J. C.; Wang, Y. Development of novel catalysts for Fischer–Tropsch synthesis: Tuning the product selectivity. *ChemCatChem* **2010**, *2*, 1030–1058.

[4] Sun, J.; Yang, G. H.; Peng, X. B.; Kang, J. C.; Wu, J. H.; Liu, G. B.;

Tsubaki, N. Beyond cars: Fischer–Tropsch synthesis for non-automotive applications. *ChemCatChem* **2019**, *11*, 1412–1424.
[5] Li, J.; He, Y. L.; Tan, L.; Zhang, P. P.; Peng, X. B.; Oruganti, A.; Yang, G. H.; Abe, H.; Wang, Y.; Tsubaki, N. Integrated tuneable synthesis of liquid fuels via Fischer–Tropsch technology. *Nat. Catal.* **2018**, *1*, 787–793.
[6] Yang, M.; Zhu, L. J.; Zhuo, Y. X.; Liang, J. C.; Wang, S. R. Selective Fischer–Tropsch synthesis for jet fuel production over Y^{3+} modified Co/H-β catalysts. *Sustain. Energy Fuels* **2020**, *4*, 3528–3536.
[7] Lin, T. J.; An, Y. L.; Yu, F.; Gong, K.; Yu, H. L.; Wang, C. Q.; Sun, Y. H.; Zhong, L. S. Advances in selectivity control for Fischer–Tropsch synthesis to fuels and chemicals with high carbon efficiency. *ACS Catal.* **2022**, *12*, 12092–12112.
[8] Li, J.; Yang, G. H.; Yoneyama, Y.; Vitidsant, T.; Tsubaki, N. Jet fuel synthesis via Fischer–Tropsch synthesis with varied 1-olefins as additives using Co/ZrO_2–SiO_2 bimodal catalyst. *Fuel* **2016**, *171*, 159–166.
[9] Li, J.; Sun, J.; Fan, R. G.; Yoneyama, Y.; Yang, G. H.; Tsubaki, N. Selectively converting biomass to jet fuel in large-scale apparatus. *ChemCatChem* **2017**, *9*, 2668–2674.
[10] Chen, Y. P.; Batalha, N.; Marinova, M.; Impéror-Clerc, M.; Ma, C. R.; Ersen, O.; Baaziz, W.; Stewart, J. A.; Curulla-Ferré, D.; Khodakov, A. Y. et al. Ruthenium silica nanoreactors with varied metal-wall distance for efficient control of hydrocarbon distribution in Fischer–Tropsch synthesis. *J. Catal.* **2018**, *365*, 429–439.
[11] Xie, R. Y.; Wang, H.; Gao, P.; Xia, L.; Zhang, Z. Z.; Zhao, T. J.; Sun, Y. H. Core@shell Co_3O_4@C-m-SiO_2 catalysts with inert C modified mesoporous channel for desired middle distillate. *Appl. Catal. A* **2015**, *492*, 93–99.
[12] Pan, X. L.; Fan, Z. L.; Chen, W.; Ding, Y. J.; Luo, H. Y.; Bao, X. H. Enhanced ethanol production inside carbon-nanotube reactors containing catalytic particles. *Nat. Mater.* **2007**, *6*, 507–511.
[13] Yuan, Y.; Huang, E. W.; Hwang, S.; Liu, P.; Chen, J. G. Confining platinum clusters in indium-modified ZSM-5 zeolite to promote propane dehydrogenation. *Nat. Commun.* **2024**, *15*, 6529.
[14] Shen, Z.; Chen, G. H.; Cheng, X. Y.; Xu, F. F.; Huang, H. W.; Wang, X. Z.; Yang, L. J.; Wu, Q.; Hu, Z. Self-enhanced localized alkalinity at the encapsulated Cu catalyst for superb electrocatalytic nitrate/nitrite reduction to NH_3 in neutral electrolyte. *Sci. Adv.* **2024**, *10*, eadm9325.
[15] Liu, J.; Wickramaratne, N. P.; Qiao, S. Z.; Jaroniec, M. Molecular-based design and emerging applications of nanoporous carbon spheres. *Nat. Mater.* **2015**, *14*, 763–774.
[16] Tavakkoli, M.; Kallio, T.; Reynaud, O.; Nasibulin, A. G.; Johans, C.; Sainio, J.; Jiang, H.; Kauppinen, E. I.; Laasonen, K. Single-shell carbon-encapsulated iron nanoparticles: Synthesis and high electrocatalytic activity for hydrogen evolution reaction. *Angew. Chem., Int. Ed.* **2015**, *54*, 4535–4538.
[17] Yang, H. Q.; Zhang, L.; Zhong, L.; Yang, Q. H.; Li, C. Enhanced cooperative activation effect in the hydrolytic kinetic resolution of epoxides on [Co(salen)] catalysts confined in nanocages. *Angew. Chem., Int. Ed.* **2007**, *46*, 6861–6865.
[18] Wu, Q.; Yang, L. J.; Wang, X. Z.; Hu, Z. Carbon-based nanocages: A new platform for advanced energy storage and conversion. *Adv. Mater.* **2020**, *32*, 1904177.
[19] Dry, M. E. The Fischer–Tropsch process: 1950–2000. *Catal. Today* **2002**, *71*, 227–241.
[20] de Klerk, A. Can Fischer–Tropsch syncrude be refined to on-specification diesel fuel. *Energy Fuels* **2009**, *23*, 4593–4604.
[21] Zhang, M. T.; Wang, M.; Xu, B. J.; Ma, D. How to measure the reaction performance of heterogeneous catalytic reactions reliably. *Joule* **2019**, *3*, 2876–2883.
[22] Zhuo, O.; Yang, L. J.; Gao, F. J.; Xu, B. L.; Wu, Q.; Fan, Y. N.; Zhang, Y.; Jiang, Y. F.; Huang, R. S.; Wang, X. Z. et al. Stabilizing the active phase of iron-based Fischer–Tropsch catalysts for lower olefins: Mechanism and strategy. *Chem. Sci.* **2019**, *10*, 6083–6090.
[23] Wikipedia. "Surface sensitivity", can be found under [Online]. https://en.wikipedia.org/wiki/X-ray_photoelectron_spectroscopy (accessed Sep 12, 2024).
[24] Torres Galvis, H. M.; Bitter, J. H.; Davidian, T.; Ruitenbeek, M.; Dugulan, A. I.; de Jong, K. P. Iron particle size effects for direct production of lower olefins from synthesis Gas. *J. Am. Chem. Soc.* **2012**, *134*, 16207–16215.
[25] Yang, C.; Zhao, H. B.; Hou, Y. L.; Ma, D. Fe_5C_2 nanoparticles: A facile bromide-induced synthesis and as an active phase for Fischer–Tropsch synthesis. *J. Am. Chem. Soc.* **2012**, *134*, 15814–15821.
[26] Zhai, P.; Xu, C.; Gao, R.; Liu, X.; Li, M. Z.; Li, W. Z.; Fu, X. P.; Jia, C. J.; Xie, J. L.; Zhao, M. et al. Highly tunable selectivity for syngas-derived alkenes over zinc and sodium-modulated Fe_5C_2 catalyst. *Angew. Chem., Int. Ed.* **2016**, *55*, 9902–9907.
[27] Yang, Y.; Xiang, H. W.; Xu, Y. Y.; Bai, L.; Li, Y. W. Effect of potassium promoter on precipitated iron-manganese catalyst for Fischer–Tropsch synthesis. *Appl. Catal. A* **2004**, *266*, 181–194.
[28] Nakhaei Pour, A.; Housaindokht, M. R.; Irani, M.; Kamali Shahri, S. M. Size-dependent studies of Fischer–Tropsch synthesis on iron based catalyst: New kinetic model. *Fuel* **2014**, *116*, 787–793.
[29] Huo, C. F.; Wu, B. S.; Gao, P.; Yang, Y.; Li, Y. W.; Jiao, H. J. The mechanism of potassium promoter: Enhancing the stability of active surfaces. *Angew. Chem., Int. Ed.* **2011**, *50*, 7403–7406.
[30] Guan, J.; Pan, X. L.; Liu, X.; Bao, X. H. Syngas segregation induced by confinement in carbon nanotubes: A combined first-principles and Monte Carlo study. *J. Phys. Chem. C* **2009**, *113*, 21687–21692.
[31] Pan, X. L.; Bao, X. H. The effects of confinement inside carbon nanotubes on catalysis. *Acc. Chem. Res.* **2011**, *44*, 553–562.
[32] Bai, S. Y.; Li, B.; Peng, J.; Zhang, X. M.; Yang, Q. H.; Li, C. Promoted activity of Cr(Salen) in a nanoreactor for kinetic resolution of terminal epoxides. *Chem. Sci.* **2012**, *3*, 2864–2867.
[33] Wu, W. L.; Luo, J. H.; Zhao, J. K.; Wang, M. L.; Luo, L.; Hu, S. P.; He, B. X.; Ma, C.; Li, H. L.; Zeng, J. Facet sensitivity of iron carbides in Fischer–Tropsch synthesis. *Nat. Commun.* **2024**, *15*, 6108.
[34] Li, Y. B.; He, Y. L.; Fujihara, K.; Gu, Y. Q.; Gao, W. Z.; Yasuda, S.; Yang, G. H.; Tsubaki, N. Directly Converting CO_2 to light hydrocarbons on a FeCoAl Prussian blue analogue-based core–shell catalyst via Fischer–Tropsch synthesis. *ACS Catal.* **2023**, *13*, 12174–12185.
[35] Schulz, H. Short history and present trends of Fischer–Tropsch synthesis. *Appl. Catal. A* **1999**, *186*, 3–12.
[36] Shen, L. M.; Sun, T.; Zhuo, O.; Che, R. C.; Li, D. Q.; Ji, Y. C.; Bu, Y. F.; Wu, Q.; Yang, L. J.; Chen, Q. et al. Alcohol-tolerant platinum electrocatalyst for oxygen reduction by encapsulating platinum nanoparticles inside nitrogen-doped carbon nanocages. *ACS Appl. Mater. Interfaces* **2016**, *8*, 16664–16669.
[37] Zhao, J.; Fan, H.; Li, G. C.; Wu, Q.; Yang, L. J.; Ma, Y. W.; Wang, X. Z.; Hu, Z. Enlarging ion-transfer micropore channels of hierarchical carbon nanocages for ultrahigh energy and power densities. *Sci. China Mater.* **2021**, *64*, 2173–2181.